Journal of Energy Storage 122 (2025) 116313

Contents lists available at ScienceDirect

Journal of Energy Storage

journal homepage: www.elsevier.com/locate/est

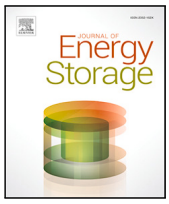

Research papers

A transformer-enhanced framework for lithium-ion battery capacity estimation using limited imaginary impedance feature☆

Ruijun Liu [a], Dayu Zhang [b,*], Lu Wang [c], Chunting Chris Mi [d], Pavol Bauer [a], Zian Qin [a,*]

[a] Department of Electrical Sustainable Energy, Delft University of Technology, Delft, 2628 CD, The Netherlands
[b] National Engineering Research Center of Electric Vehicles, Beijing Institute of Technology, Beijing, 100081, China
[c] Hitachi Energy Sweden AB - Research Center,, Västerås, 72226, Sweden
[d] Electrical and Computer Engineering, San Diego State University, San Diego, CA 92182, USA

ARTICLE INFO

Keywords:
Lithium-ion battery
Electrochemical impedance spectroscopy
Capacity estimation
Deep learning

ABSTRACT

Accurate battery capacity estimation is essential for the effective and reliable operation of lithium-ion battery management systems. Battery impedance is a key parameter that encapsulates electrochemical information, closely correlating with the internal states of batteries. This study proposes a novel capacity estimation framework that effectively balances accuracy, efficiency, and practicality. Firstly, a novel feature extraction method is introduced to extract health features from the imaginary impedance at a single frequency. The extracted feature demonstrates a strong and stable correlation with battery degradation under various operation conditions, while significantly reducing data requirements. To address the impact of diverse degradation patterns on estimation accuracy, an initial adjustment method is applied to precisely retrace the relative degradation paths of batteries. The results show that the mean absolute percentage error of battery capacity estimation decreases from 15.65% to 2.87%. Additionally, a transformer-based capacity estimation model is developed, which integrates a feature fusion unit to explicitly eliminate the influence of temperature on model performance. As a result, the model's accuracy improves by over 28% under various thermal conditions.

1. Introduction

Lithium-ion batteries, known for their high energy density, rapid charging and discharging capabilities, long lifespan, and less memory effect, have become an indispensable component in electronic devices, energy storage systems, and transportation fields [1]. However, the inherent characteristics of electrochemical systems result in inevitable degradation of the battery over time, whether during usage or storage [2]. As batteries age with use, their performance gradually declines, making it necessary to monitor and evaluate their condition to prevent unexpected failures. To ensure the safe and reliable use of batteries and to optimize the timing for battery replacement, accurately assessing the degradation status of the battery is both crucial and widely regarded as a significant area of interest.

Therefore, we rely on the parameter 'State of Health' (SOH) to assess the battery's health and ensure its performance and safety. Typically, the SOH of a battery is defined as the ratio of current capacity to initial capacity. When the SOH decreases to around 80%, the battery is considered to have reached the end of its life [3,4]. However, degradation mechanisms — such as solid electrolyte interphase growth, lithium plating, and particle cracking — lead to irreversible loss of lithium-ion inventory and active materials. Most existing measurement methods for quantifying the progress and rates of the degradation processes are destructive to the battery or necessitate expensive detectors and stable operating conditions [5,6]. Consequently, extensive research has focused on leveraging more accessible data to assess battery health status, which can be generally categorized into model-based and data-driven methods [7–9]. Model-based methods involve constructing mathematical models based on the physical properties of batteries and experimental data. These models aim to describe battery degradation behavior and provide a descriptive expression for the variation of battery performance over its lifetime. [10]. Among model-based methods, electrochemical models, equivalent circuit models (ECM), and state-space estimation techniques such as Kalman filters are widely discussed [11,12]. Electrochemical model capture the internal aging processes within the battery from a microscopic perspective

☆ ECS4DRES is supported by the Chips Joint Undertaking, grant agreement number 101139790 and its members, including the top-up funding by Germany, Italy, Slovakia, Spain and The Netherlands.

* Corresponding authors.
E-mail addresses: dayu_zhang@bit.edu.cn (D. Zhang), Z.Qin-2@tudelft.nl (Z. Qin).

https://doi.org/10.1016/j.est.2025.116313
Received 8 November 2024; Received in revised form 25 February 2025; Accepted 17 March 2025
Available online 20 April 2025

using partial differential equations, providing a solid physical basis [13,14]. Kalman filter-based approaches, including variants such as the extended Kalman filter and unscented Kalman filter, leverage state-space representations to estimate key battery parameters like state-of-charge (SOC) and SOH in real time [15]. These methods incorporate measurement updates to correct system predictions, enhancing robustness in practical applications [12,16]. ECM employs electronic components such as resistors and capacitors to simulate the external electrical characteristics of the battery, which reduces computational costs but limits estimation accuracy [17,18]. For model-based methods, the modeling process typically involves numerous parameters, some of which require specialized sensors for measurement. Moreover, these models often exhibit poor scalability, as they are primarily developed in controlled laboratory environments, raising concerns about their adaptability to complex real-world applications.

Given the complexity of the battery degradation mechanism, a promising approach for accurately estimating SOH is through data-driven methods, which have become a focus in recent years. [19–22]. Similar to the other complexity processes, e.g., natural language processing, modeling the battery degradation with data-driven approaches avoids physically describing the mechanism behind [23]. Instead, the pattern of battery degradation is extracted directly from the monitored data. Representative algorithms include convolutional neural networks (CNN) [24], which are employed by the authors to extract indicators for achieving accurate SOH estimation. Recurrent neural network (RNN) and long short-term memory (LSTM) algorithms are widely used in battery aging modeling [21,22] to process time series data and obtain real-time capacity predictions. However, these algorithms have limitations in parallel computing performance. In contrast, the Transformer [25–27], with its self-attention mechanism, excels at parallel processing and demonstrates great potential in handling long sequence data, making it a promising approach for battery aging trend prediction. Additionally, generative adversarial networks (GAN) represent another noteworthy approach, as introduced in [28]. In this method, features extracted by GAN are fed into Gaussian process regression (GPR) for capacity estimation. However, this feature selection method is relatively complex.

For the sake of achieving high estimation accuracy with machine learning techniques, feature extraction plays a crucial role in estimating the SOH of batteries. The feature extraction methods can be roughly divided into two categories: the indirect analysis method and the direct measurement method [29]. Indirect analysis methods require the analysis and processing of data to generate features related to SOH, which is a typical multi-step deduction method. Among them, the charging curve method [21,30,31], incremental capacity, and differential voltage method [32–34] have been extensively explored for battery health prognostics. However, the aforementioned methods typically exhibit significant dependence on operating conditions and need to be conducted under specific testing parameters, such as low current rates and constant temperatures. Moreover, variations in data processing approaches can significantly affect the effectiveness of feature extraction in these methods [35]. In contrast, the direct measurement method refers to the specific calculation and measurement of relevant parameters of the battery, including ohmic resistance and electrochemical impedance spectroscopy (EIS) measurement [26,28,36,37]. Compared to indirect methods, the direct measurement method is simpler and more direct, avoiding the complex calculations and potential errors associated with data processing. Specifically, when carrying EIS measurement, the battery input impedance is measured via injecting small sinusoidal voltage perturbations at a certain frequency into the battery and measuring the responding current at the same frequency. Compared to other measurement parameters, EIS can directly reflect changes in battery aging mechanisms [35]. Therefore, EIS has attracted considerable attention for estimating battery health [19,26,28,36–39]. Among them, [26] proposed a simple EIS feature extraction method, utilizing EIS measurements at five representative frequencies as features for SOH estimation. Although this approach reduces the volume of broadband EIS data, the selection of these frequencies varies depending on different battery types, operating conditions, and temperatures. Moreover, the amount of data collected at these five frequencies is substantial. [28] used a generative adversarial network to select features from EIS data, which requires less data but the feature extraction is relatively complex and ignores the effect of temperature changes on battery aging curves. In [37], Jiang et al. conducted a comparative study on SOH estimation using EIS data, considering three situations: broadband EIS, ECM, and fixed frequency. However, the influence of temperature and SOC changes is not fully considered, and high similarity is observed among training and testing samples. These limitations in dataset diversity diminish the generalizability and robustness of the methods.

Table 1
Different states during CC-CV charging and discharging.

State	Description	Resting	DC	SOC
1	Before charging	✓	–	0%
2	After 20-min charging	–	✓	≈40%
3	After charging and before resting	–	–	≈100%
4	After 15-min rest	✓	–	100%
5	After 10-min discharging	–	✓	≈40%
6	After 15-min rest	✓	–	0%

Although existing research has made significant progress in battery health assessment, there are still some research gaps. These include insufficiently effective and comprehensive feature selection, the uncertainty of constructed models to batteries with diverse degradation patterns, and a lack of consideration for temperature and SOC effects. This work aims to address the above-mentioned research questions: 1. How to obtain features from EIS that adapt to various working states; 2. How to eliminate the influence of significant degradation pattern differences on model accuracy; 3. How to improve the model performance in various temperature conditions. To address these research gaps, this paper proposes a feasible framework that extracts features from the imaginary impedance at a specific frequency for estimating capacity under various temperature conditions and degradation patterns. The main contributions are summarized as follows

1. A new feature extraction strategy is proposed, which effectively reduces the complexity of feature engineering while improving prediction accuracy. Specifically, the analysis reveals that the feature extracted based on the imaginary impedance at a specific frequency exhibit a strong correlation with battery degradation. Moreover, these features demonstrate robust performance across different operating conditions, significantly enhancing their practical applicability.
2. An effective pre-processing method is proposed to eliminate significant discrepancies in degradation patterns among batteries, enabling more accurate capture of relative evolution trends. Specifically, generalization across different battery cells of the same type is enhanced through an initial adjustment method, which mitigates variations in initial conditions before training, thereby improving model robustness and estimation accuracy.
3. A transformer-based estimation model is established, effectively incorporating temperature effects to enhance accuracy under varying temperature conditions. Specifically, a feature fusion unit is introduced to explicitly consider temperature influence on capacity estimation, improving sensitivity to temperature variations.

The workflow of this study is shown in Fig. 1. The remainder of this study is organized as follows: Section 2 introduces the dataset used in this work. Subsequently, the feature extraction method and the initial adjustment method are illustrated. In Section 3, the transformer-based temperature-enhanced model is demonstrated in detail. Capacity estimation results and comparison cases are provided in Section 4. Finally, the conclusions are summarized in Section 5. A comprehensive list of all abbreviations employed in this study can be found in Appendix Table A.4.

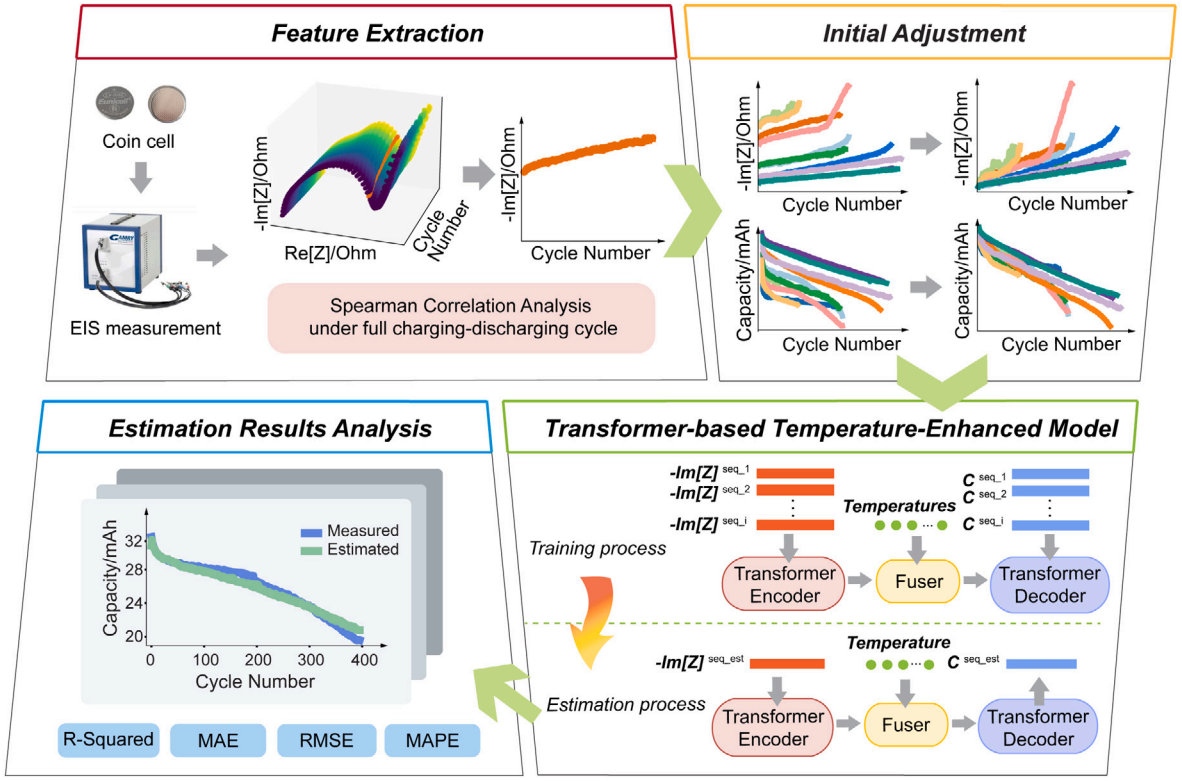

Fig. 1. The workflow of the proposed method.

2. Data analysis and feature extraction

In this section, a detailed introduction is provided to the battery degradation dataset used in this work. Subsequently, the feature extraction method related to EIS and the initial adjustment method for handling significant data discrepancies will be discussed.

2.1. Battery degradation experimental data analysis

The experimental dataset used in this research is available from the University of Cambridge [19], featuring cells with a LiCoO2/graphite chemistry. These cells were subjected to cycling at three distinct temperatures: 25 °C (T251-T256), 35 °C (T351 and T352), and 45 °C (T451 and T452), respectively. In this study, ten batteries are divided into a training set (T251, T253, T254, T351, T352), a validation set (T252), and a test set (T255, T256, T352, T452). A constant current-constant voltage (CC-CV) profile is used to charge the tested battery cells to their upper cut-off voltage (4.2 V) with a current of 1C rate. After resting for 15 min, the battery was discharged with a current of 2C rate to its lower cut-off voltage, which forms a complete test cycle, as shown in Fig. 2. EIS measurements were conducted across six states during the charging and discharging processes. For each state, EIS was measured across a frequency range from 0.02 Hz to 20 kHz, sampling 60 distinct frequencies to capture both the real Re(Z) and imaginary Im(Z) components of impedance Z. Table 1 outlines six states based on the battery's states during charging and discharging cycles, including whether there is resting or direct current (DC), and the state of charge (SOC). For Resting and DC, '✓' indicates presence and '–' indicates absence.

2.2. EIS-related feature extraction

This study focuses on six operational states of the battery cells, covering four representative phases throughout the full charging and discharging process, ensuring that the research results possess broad applicability.

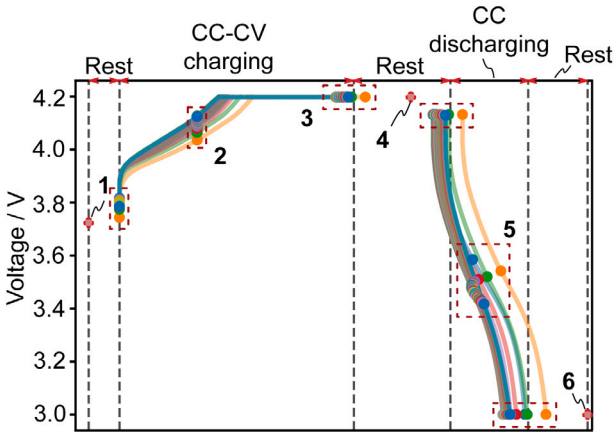

Fig. 2. Different states during CC-CV charging and discharging.

a. State 1: At this time, the battery is in an open circuit state, the internal chemical reactions of the battery are in a state of equilibrium, and relatively accurate battery parameters can be obtained [40].
b. State 2: In this state, the battery is in the charging process, with the SOC approximately at 40%. In practical scenarios, charging a battery to 40% SOC is a common phase [41]. Selecting this state for feature extraction improves the feasibility of the proposed method in practical application.
c. State 3: When the battery is fully charged, its voltage has reached the manufacturer's specified maximum charging voltage, and the internal chemical reactions are nearly in equilibrium. At this point, the battery's parameters are also relatively stable.
d. State 4: In which state the battery was fully charged and allowed to rest for 15 min. This rest period helps mitigate internal thermal effects and voltage relaxation, providing a more stable condition for accurate measurement of charging capacity [42].

e. State 5: During this phase, the battery is discharged from 100% SOC to about 40%, with a constant current of 2C. Similar to state 2, this state was selected because discharging a battery to approximately 40% SOC is a common and achievable daily-use condition. The features extracted from this state are thus highly applicable. It should be noted that data from battery cells T253, T255, and T256 are exclusively available for State 5.
f. State 6: In this state, the battery has been fully discharged and then left to rest for 15 min to achieve stable conditions for discharge capacity measurement.

After introducing these states, it is necessary to analyze each state's EIS and capacity data. However, not all EIS is relevant to battery ageing. Specifically, the EIS data at some frequencies are more sensitive to battery ageing than others. To reduce computational cost and the time cost of model training, only the EIS data showing a high correlation with battery ageing is selected as a feature.

The EIS data of ten battery cells, including both real and imaginary impedance at 60 different frequencies, have been selected for this study. The discharge capacity of each cycle is utilized to represent the current capacity status. To extract the EIS data most relevant to battery aging, it is essential to perform a correlation analysis between the real and imaginary impedance at all 60 frequencies against the capacity for each cell. Before conducting the correlation analysis, it is necessary to verify whether the impedance sequences at varying frequencies and the capacity data adhere to a normal distribution [43]. Employing the Shapiro–Wilk test, it was discovered that almost all data sets in the study had p-values significantly below the standard significance level (typically 0.05), indicating that the tested data do not follow a normal distribution. For data that does not conform to a normal distribution and has nonlinear relationships, the Spearman's rank correlation coefficient (SCC) is utilized in this research to evaluate the interrelationships between feature and capacity quantitatively [44], which is derived as Eq. (1):

$$r_s = \rho_{\text{Spearman}} = \frac{\text{cov}(R(X), R(Y))}{\sigma_{R(X)}\sigma_{R(Y)}} \tag{1}$$

where cov(*R(X)*, *R(Y)*) represents the covariance of the ranks of variables X and Y. $\sigma_{R(X)}$ and $\sigma_{R(Y)}$ are the standard deviations of the ranks of variables X and Y, respectively. X is the feature sequence and Y is the battery discharging capacity sequence.

According to the correlation analysis in Fig. 3, the calculated Spearman's rank correlation coefficients between the EIS data at different frequencies and capacity for ten batteries are presented. The values of the correlation coefficients range from 0 to 1, where 1 indicates a perfect correlation and 0 indicates no correlation. Fig. 3(a–f) represents the correlation coefficients between Re[Z] and capacity at six selected states, respectively, while Fig. 3(g–l) demonstrate the correlations between -Im[Z] and capacity at corresponding state. In each subplot, the horizontal axis represents 60 frequencies, and the vertical axis is the number of the ten selected batteries. The impedance sequences with absolute correlation coefficients exceeding 0.85 are deemed to have a strong correlation with capacity, which is outlined by the pink box in Fig. 3. It is evident that no consistent frequency regions exhibit uniform correlations across all ten batteries within the real part of impedance sequences. However, for the imaginary part of the impedance sequences, each state reveals a fixed region where the absolute value of the correlation coefficient is greater than 0.85, with these regions showing overlap across the four states. Thus, it can be inferred that the imaginary part of impedance sequences between 2.74 Hz and 4.37 Hz strongly correlates with the discharge capacity sequences and exhibits significant consistency across all ten batteries and four states. In subsequent research presented in this paper, the imaginary part of impedance at a frequency of 2.74 Hz is selected as the subject of study.

2.3. Initial adjustment for data discrepancies

After extracting the imaginary impedance data at the frequency of 2.74 Hz, an analysis through graphical representation revealed considerable variation within the dataset. As shown in Fig. 4(a), the range of -Im[Z] values for ten batteries was 0.02 ∼ 0.28 Ω, with the maximum difference within the same cycle reaching 0.23Ω. Fig. 4(b) illustrates that the range of capacity for the batteries spanned 20 ∼ 42 mAh, with the maximum difference in the same cycle reaching 13 mAh and a maximum cycle difference of 480 at the same capacity level. Fig. 4(c) shows that the maximum discrepancy in -Im[Z] values could reach 0.15Ω when the capacity values were consistent. These significant variations in battery degradation curves stem primarily from manufacturing inconsistencies, which result in differences in initial capacity and degradation rates. Previous studies have reported similar initial capacity disparities in this dataset [26,28,45–47]. Such variations, commonly attributed to electrode thickness, electrolyte distribution, and formation process inconsistencies [48,49], pose challenges for accurate capacity estimation.

To eliminate the significant disparities between different batteries and characterize degradation trends of batteries more intuitively, we introduce the initial adjustment method, which is demonstrated in Eq. (2).

$$\Delta X_i(t) = X_i(t) - X_i(0) \tag{2}$$

where $X_i(t)$ is the original sequence data of capacity/-Im[Z], $X_i(0)$ is the initial data of capacity/-Im[Z].

This method subtracts the first data point from each value in the original data series, emphasizing the relative changes in capacity and imaginary impedance due to battery aging. Since Spearman correlation is based on ranks rather than absolute values, subtracting the initial values does not affect the real correlation between features and capacity. As illustrated in Fig. 4(d), after the initial adjustment, the maximum difference at the same cycle decreased to 0.13Ω, nearly halving the original value. Fig. 4(e) shows that the maximum difference at the same cycle reduced from 10 mAh to 3 mAh, with the maximum cycle discrepancy at the same capacity level decreasing to 280 cycles. Furthermore, Fig. 4(f) indicates that the maximum discrepancy in -Im[Z] values under consistent capacity conditions was reduced to 0.09Ω, a decrease of 0.06Ω from the original data. With the data range more concentrated through initial adjustment, subsequent modeling can focus more on the aging process rather than being influenced by the significant initial value discrepancies, thereby enhancing the accuracy of capacity estimation.

3. Transformer architecture with temperature-enhanced feature fusion

3.1. Padding and masking

In this dataset, the number of cycles required for each battery to reach its end of life (EoL) varies significantly, with some batteries differing by more than 400 cycles. This presents a challenge for deep learning frameworks like TensorFlow or PyTorch, which rely on batch processing and require consistent input dimensions for parallel computation. To address this, shorter battery sequences are padded with zeros at the end, ensuring that all sequences match the length of the longest battery sequence. To prevent these zero paddings from affecting the modeling of battery degradation, a masking matrix is generated. This matrix integrates with the computation of attention scores, assigning negative infinity to the scores at masked positions, thereby reducing their influence and ensuring that the attention weights for these positions are effectively zero. It is important to note that padding and masking are only necessary during the model training phase. Once the model is being tested, or when it is used as a trained model in real-life applications, it can accept inputs of any shape.

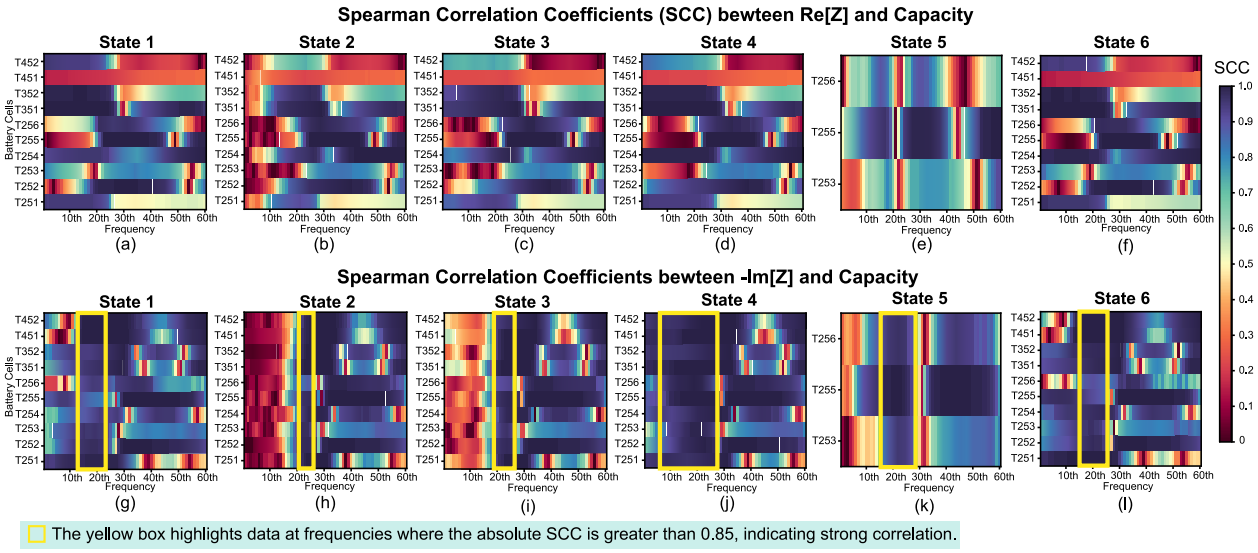

Fig. 3. Spearman correlation analysis results for 10 battery cells. Correlation coefficient between Re[Z] and Capacity in (a) state 1. (b) state 2. (c) state 3. (d) state 4. (e) state 5. (f) state 6. Correlation coefficient between -Im[Z] and Capacity in (g) state 1. (h) state 2. (i) state 3. (j) state 4. (k) state 5. (i) state 6.

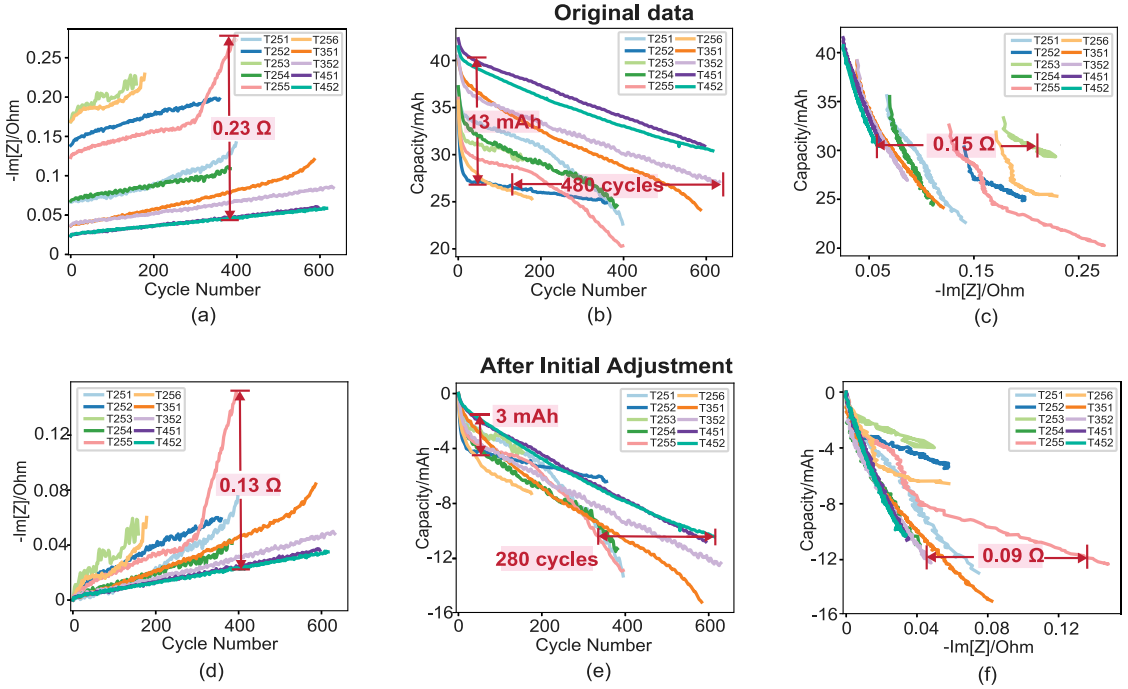

Fig. 4. Original data and data after initial adjustment for 10 battery cells: (a) original -Im[Z] data. (b) original capacity data. (c) relationship graph between original -Im[Z] and original capacity. (d) -Im[Z] data after initial adjustment. (e) capacity data after initial adjustment. (f) relationship graph between -Im[Z] and original capacity after initial adjustment.

3.2. Encoder-fuser-decoder framework

The fundamental concept of the encoder–decoder framework is to map one-time series to another while integrating additional information about operational conditions. In this study, we use the imaginary part of the impedance, -Im[Z], as the input sequence and the capacity as the output sequence. However, both the impedance and capacity of the battery are significantly influenced by temperature. As the battery ages, its impedance and capacity exhibit different trends under various operation temperatures. Therefore, a temperature feature fusion unit is implemented between the encoder and decoder to incorporate the effects of temperature into the battery aging modeling, aiming for more accurate capacity estimation.

Fig. 5 shows the simplified structure and data flow of the proposed Encoder-Fuser-Decoder Framework. The encoder takes the -Im[Z] sequence as input and maps this sequence to a fixed-dimensional vector, capturing the sequential information and its correlation with cycle numbers. The output from the encoder is a hidden state vector that encapsulates all necessary information extracted from the input sequence, mapping it into a domain with hidden states. This hidden state vector is then fed into a fuser, which modifies it based on the temperature feature inputs. The underlying principle of the fuser is that changes in battery capacity over cycles are influenced not only by battery impedance but also by many other factors. In this paper, the focus is primarily on the influence of temperature, but the fuser could also incorporate additional factors such as depth of discharge

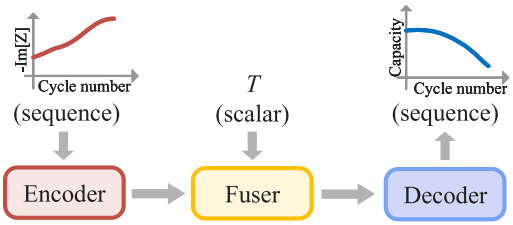

Fig. 5. Encoder-Fuser-Decoder framework diagram.

(DoD) and charge/discharge rates. Finally, the modified hidden state vector is processed by the decoder, which predicts the output sequence and capacity. During model inference, the expected response sequence is generated in an autoregressive manner, meaning each prediction is based on the current hidden state vector and all previously generated predictions, thereby preserving the temporal information of the sequence and reconstructing it sequentially with hidden temporal causality.

Encoder and decoder architectures are widely adopted for sequence-to-sequence models, such as RNN, attention-based networks (transformers), or CNN, all of which have been proven successful in handling sequential data with complex temporal correlations. In this paper, we introduce an implementation of a transformer-based architecture that enhances the traditional encoder–decoder structure by incorporating a feature fusion unit. This unit integrates temperature features to improve the accuracy of capacity estimation. In the following subsection, we provide a detailed description of this architecture to guide its application in the industrial field.

3.3. Transformer-based temperature-enhanced model

The Transformer model, a recently developed and widely used architecture, excels in modeling sequence-to-sequence tasks. Unlike RNN and LSTM, the transformer avoids recursive connections. It relies on attention mechanisms to capture temporal dependencies both within and between input and output sequences, allowing for the parallel processing of all elements in the sequence and reducing model bias concerning the order of data input. This work introduces a feature fusion unit into the standard transformer architecture to enhance its application in capacity estimation tasks. The network architecture is depicted in Fig. 6, and Table 2 provides a detailed algorithmic description.

3.3.1. Multi-head attention

The architecture utilized in this paper includes three multi-head attention modules, each comprising four self-attention mechanisms. For each element in the sequence, self-attention calculates the attention weights with all other elements in the sequence, including itself, to determine the significance of other elements to the current one [25]. Initially, each element of the sequence is projected into three spaces to form three types of vectors: query, key, and value, as shown in Eqs. (3)–(5):

$$q_i = x_i W_q \tag{3}$$

$$k_i = x_i W_k \tag{4}$$

$$v_i = x_i W_v \tag{5}$$

where x_i is the element in sequences, $W_q \in \mathbb{R}^{d_{\text{model}} \times d_k}$, $W_k \in \mathbb{R}^{d_{\text{model}} \times d_k}$, $W_v \in \mathbb{R}^{d_{\text{model}} \times d_v}$ are three parameter matrices.

Attention scores are initially computed by taking the dot product of the query vectors with the key vectors. These scores are then normalized using the softmax function, transforming them into attention weights that sum to one, making them suitable for probabilistic interpretation. The equation for calculating attention weights is shown in Eq. (6):

$$\text{Attention}(Q, K, V) = \text{softmax}\left(\frac{QK^T}{\sqrt{d_k}}\right)V \tag{6}$$

where d_k is the dimension of the key vectors. Division by $\sqrt{d_k}$ is used to scale the resulting dot product to ensure it remains within a reasonable numerical range. The final output of this process captures the relative importance of each element in the sequence, indicating how much attention the current element should pay to others.

In multi-head attention, each head computes attention weights independently, and the outputs of each head are concatenated and subsequently transformed through a trained linear transformation to integrate the learning results from different heads into a final output.

$$\begin{aligned}\text{MultiHead}(Q, K, V) &= \text{Concat}(\text{head}_1, \ldots, \text{head}_h)W_O \\ \text{where head}_i &= \text{Attention}(QW_q, KW_k, VW_v)\end{aligned} \tag{7}$$

In Eq. (7), $W_O \in \mathbb{R}^{hd_v \times d_{\text{model}}}$ is parameter matrix. In this study, h represents the number of heads, which is 4.

Table 2
Transformer architecture with temperature-enhanced feature fusion.

Algorithm Transformer-based Encoder-Fuser-Decoder Model

Input Data:
Sequences of the changes in the imaginary part of impedance with cycle numbers ***-Im(n)***, Temperature ***T***, sequences of the changes in capacity with cycle numbers ***C(n)*** (utilized only during training process);
Output Data:
Capacity;
Algorithm Flow

Step 1: *-Im'(n)* ← *-Im(n)*	[Padding & Masking]
Step 2: $X \leftarrow$ Input Layer(*-Im'(n)*)	[Mapping]
Step 3: $X \leftarrow X +$ Positional Encoding	[Encoder]
Step 4: $X \leftarrow \text{Norm}(X + \text{Multi-Head Attention}(X))$	[Encoder]
Step 5: $X \leftarrow \text{Norm}(X + \text{FNN}_1(X))$	[Encoder]
Step 6: $X' \leftarrow \text{Norm}(X + \text{FNN}_2(X, T))$	[Fuser]
Step 7: **if** training **then**	
7.1: *C'(n)* ← *C(n)*	[Padding & Masking]
7.2: $Y \leftarrow$ Input Layer(*C'(n)*)	[Mapping]
7.3: $Y \leftarrow Y +$ Positional Encoding	[Decoder]
7.4: $Y' \leftarrow \text{Norm}(Y + \text{Masked Multi-Head Attention}(Y))$	[Decoder]
7.5: $Y' \leftarrow \text{Norm}(Y + \text{Cross Multi-Head Attention}(X', Y))$	[Decoder]
7.6: $Y' \leftarrow \text{Norm}(Y + \text{FNN}_3(Y'))$	[Decoder]
7.7: *C(n)* ← Output Layer(*Y'*)	[Mapping]
Step 8: **else if** testing **then**	
8.1: Initialize $H_0(n) \leftarrow 0$	
8.2: **for** $i = 1$ to L **do**	
8.2.1: $Y \leftarrow$ Input Layer($C'_{i-1}(n)$)	[Mapping]
8.2.2: $Y \leftarrow Y +$ Positional Encoding	[Decoder]
8.2.3: $Y' \leftarrow \text{Norm}(Y + \text{Masked Multi-Head Attention}(Y))$	[Decoder]
8.2.4: $Y' \leftarrow \text{Norm}(Y + \text{Cross Multi-Head Attention}(X', Y))$	[Decoder]
8.2.5: $Y' \leftarrow \text{Norm}(Y + \text{FNN}_3(Y'))$	[Decoder]
8.2.6: $C'_i(n) \leftarrow$ Output Layer(*Y'*)	[Mapping]
8.3: $C(n) \leftarrow (C(L))$	
Step 9: **return** $C(n)$	

3.3.2. Model description

Fig. 6 depicts the overall architecture of the model. The imaginary part of impedance sequences inputs, denoted as *-Im(n)*, initially undergoes padding and masking to produce padded input sequences, *-Im'(n)*, along with its mask. Each data point of *-Im'(n)* is then passed through an input layer and projected onto a d-dimensional vector, which sets the representation dimension of the model. Since the transformer model relies entirely on attention mechanisms, positional encoding is added to the input vector to provide positional information and capture temporal dependencies. The multi-head attention module then processes the sequence, computing attention scores and extracting meaningful temporal patterns. These processed vectors are passed through a feed-forward neural network (FNN), generating hidden representations,

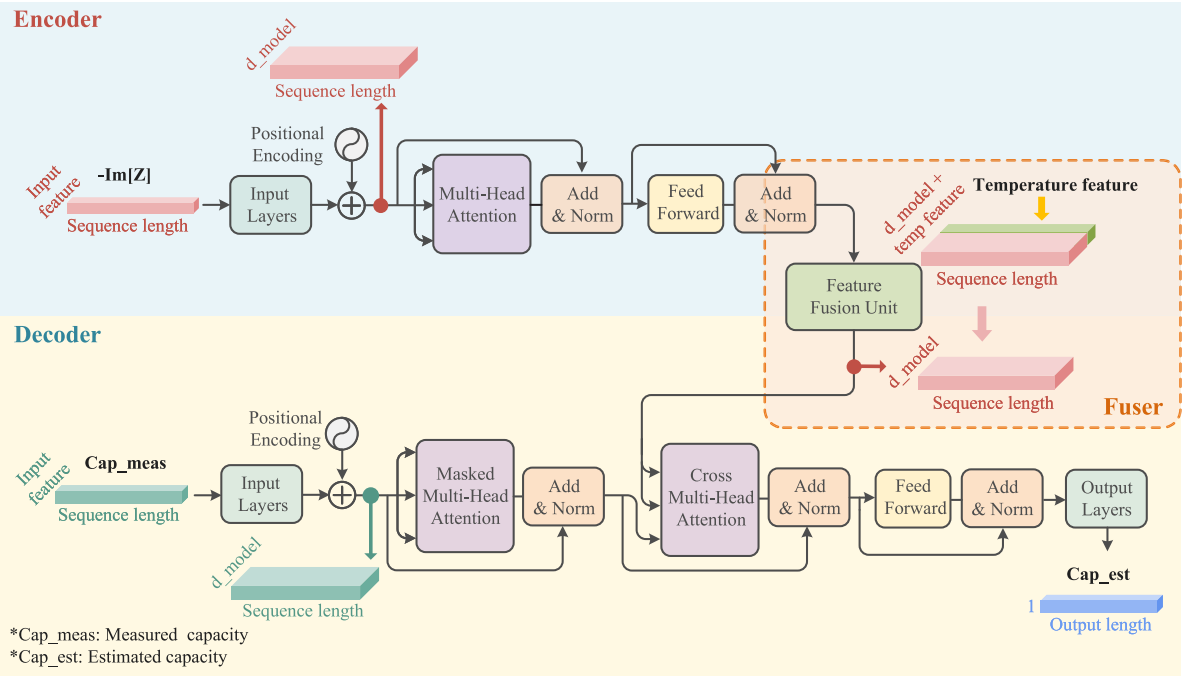

Fig. 6. Transformer architecture with temperature-enhanced feature fusion.

which are then concatenated with the temperature input and fed into the fuser. The fuser, also an FNN, applies a nonlinear transformation to incorporate temperature effects before passing the modified hidden vectors to the decoder for output reconstruction.

During training, the target capacity sequence *C(n)* undergoes padding and masking to form an input sequence *-Im'(n)*, which is mapped into a d-dimensional vector via an FNN. This vector, combined with positional encoding, is processed through a masked multi-head attention module, ensuring the model focuses on relevant sequence parts. The output is further refined using a cross-multi-head attention module, integrating information from both the fuser and decoder. Finally, a shallow FNN maps the output vectors to the estimated capacity sequence *C(n)*.

3.3.3. Performance metrics

To comprehensively validate the feasibility of the proposed SOH estimation method, the mean absolute error (MAE), root mean square error (RMSE), mean absolute percentage error (MAPE), and R-squared are employed in this study, which is defined as Eqs. (8)–(11):

$$\mathrm{MAE} = \frac{1}{n}\sum_{i=1}^{n}|y_i - \hat{y}_i| \tag{8}$$

$$\mathrm{RMSE} = \sqrt{\frac{1}{n}\sum_{i=1}^{n}(y_i - \hat{y}_i)^2} \tag{9}$$

$$\mathrm{MAPE} = \frac{1}{n}\sum_{i=1}^{n}\left|\frac{y_i - \hat{y}_i}{y_i}\right| \times 100\% \tag{10}$$

$$R^2 = 1 - \frac{\sum_{i=1}^{n}(y_i - \hat{y}_i)^2}{\sum_{i=1}^{n}(y_i - \bar{y})^2} \tag{11}$$

where y_i is the measured capacity value, $\hat{y}_i$ is the estimated capacity value, and $\bar{y}$ is the average value of the measured capacity value.

4. Estimation results and discussions

To comprehensively evaluate the performance of the proposed framework, this section presents the capacity estimation results under different states and operating temperatures. Additionally, comparisons of results under multiple cases are provided to further demonstrate the effectiveness of the proposed approach. Finally, the proposed method is compared with several common benchmark methods. Ten batteries are then trained and tested under six battery charge–discharge states. It is important to note that the source dataset for State 5 only provides data for batteries T253, T255, and T256. Hence, the first two are used for the training set and T256 as the test battery.

4.1. Capacity estimation results

Based on the conclusion drawn in Section 2.3, the imaginary impedances at 2.74 Hz were selected as individual features for each batteries, providing unique identifiers for the proposed model. Fig. 7 shows the results under fully discharged state. Table 3 presents the estimation results of this study, evaluated using four performance metrics: the percentage of RMSE, MAE, MAPE, and R^2. Fig. 8 shows the comparison between the estimated and actual battery aging curves for different charging and discharging states, using T452 as an example. Generally, the proposed method achieves excellent performance in battery capacity estimation, especially in states 1, 2, 5, and 6. In state 3 and 4, batteries T255, T352, and T452 achieve quite accurate estimation results, with the average MAPE lower than 5%, which can satisfy the real-world application requirements [51]. Specifically, battery T452 achieves higher accuracy across six states, especially in state 6, with an RMSE of only 0.6468% and an MAE of 0.2046 mAh and the R^2 value exceeds 0.99.

Since this study utilizes publicly available data, a comparison with estimation results from other studies is presented in Table 3. Ref. [28] employed a GAN-based feature selection approach followed by GPR for capacity estimation. However, this study only considered battery performance at a constant temperature of 25 °C and did not account for capacity variations under different temperature conditions. The results in [50] were obtained using an FNN, while [26] utilized impedance data at five key frequencies (including both real and imaginary components) as features for capacity estimation. Ref. [45] used variational auto-encoders to extract features from EIS data and then applied bidirectional gated recurrent Unit for capacity estimation However, experiments were conducted under a single operating condition,

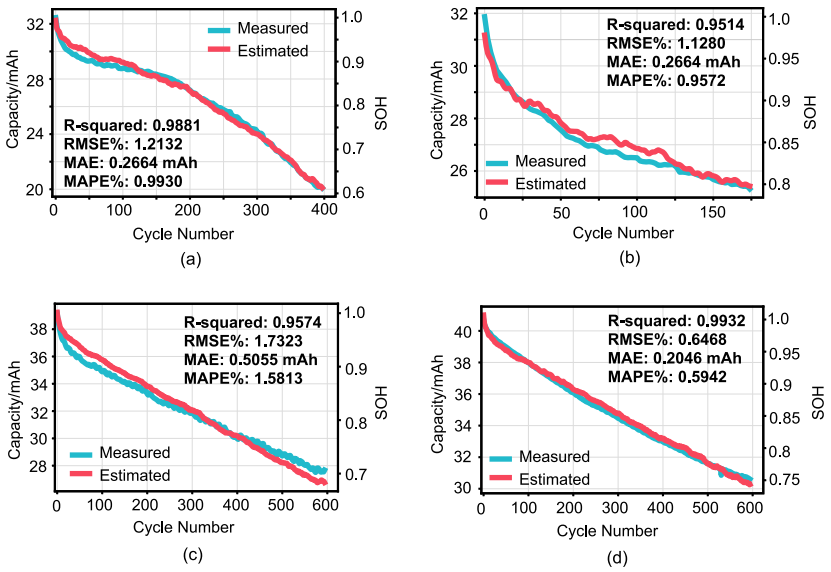

Fig. 7. Capacity estimation results in State 6 for four cells using the proposed method, (a) T255, (b) T256, (c) T352, (d) T452.

Table 3
Capacity estimation results.

State	Cell	RMSE/%		MAE/mAh		MAPE/%		R^2	
		This work	Other works	This work	Other works	This work	Other works	This work	Other works
1	T255	1.95	–	0.45	–	1.78	–	0.97	–
	T256	1.61	–	0.40	–	1.50	–	0.89	–
	T352	2.19	–	0.57	–	1.85	–	0.93	–
	T452	1.06	–	0.31	–	**0.90**	–	**0.98**	–
2	T255	2.34	–	0.53	0.97[a]	2.05	–	0.96	0.60[a]
	T256	2.63	–	0.66	0.86[a]	2.44	–	0.72	0.62[a]
	T352	1.97	1.47[e]	0.49	–	1.65	1.51[e]	0.94	0.92[e]
	T452	1.41	1.96[e]	0.45	–	**1.31**	2.27[e]	**0.97**	0.92[e]
3	T255	3.05	–	0.62	1.16[a]	2.62	–	0.91	0.42[a]
	T256	5.46	–	1.42	1.03[a]	5.35	–	−0.14	0.26[a]
	T352	1.34	–	0.33	–	1.09	–	0.97	–
	T452	1.13	–	0.29	–	**0.87**	–	**0.98**	–
4	T255	4.66	–	0.98	0.71[a]	4.07	–	0.83	0.79[a]
	T256	4.92	–	1.33	1.68[a]	4.99	–	0.01	0.07[a]
	T352	2.11	–	0.53	–	1.76	–	0.94	0.85[e]
	T452	0.82	–	0.23	–	**0.66**	–	**0.99**	0.80[f]
5	T256	3.77	–	0.98	0.72[a]	3.58	–	0.89	0.74[a]
6	T255	1.21	–	0.27	0.54[d]	0.99	–	0.99	0.96[d]
	T256	1.13	–	0.27	1.07[d]	0.96	–	0.95	0.90[d]
	T352	1.73	3.09[c]	0.51	0.97[c]	1.58	3.30[c]	0.96	0.82[c]
					0.51[b]		1.63[b]		0.94[b]
					0.30[d]				0.98[d]
	T452	0.65	1.82[c]	0.20	0.68[c]	**0.59**	2.05[c]	**0.99**	0.93[c]
					0.39[d]				0.97[b]

Note:[–] indicates data not available.
[a] Indicates the results are from [28].
[b] Indicates the results are from [26].
[c] Indicates the results are from [50].
[d] Indicates the results are from [45].
[e] Indicates the results are from [46].
[f] Indicates the results are from [47].

and the accuracy was suboptimal. The results in [46] are close to those of the proposed method, which achieves slightly better overall performance. This study, however, employs a more complex feature selection approach, involving impedance fitting with the Voigt circuit model and residual calculation, while also selecting more features than the proposed method. Ref. [47] utilized all EIS data as features and applies the complex CNN-BiLSTM model for capacity estimation. However, the final estimation results are not very satisfactory.

As shown in Table 3, the proposed framework demonstrates higher estimation accuracy compared to the methods in these studies and is applicable to a broader range of battery charging and discharging states. The referenced studies did not incorporate temperature feature fusion, resulting in lower accuracy across different temperatures. Additionally, the lack of initial adjustment led to less precise predictions when SOH was above 80%, which is particularly critical since batteries typically enter the recycling process once SOH drops to 80%. Furthermore, their

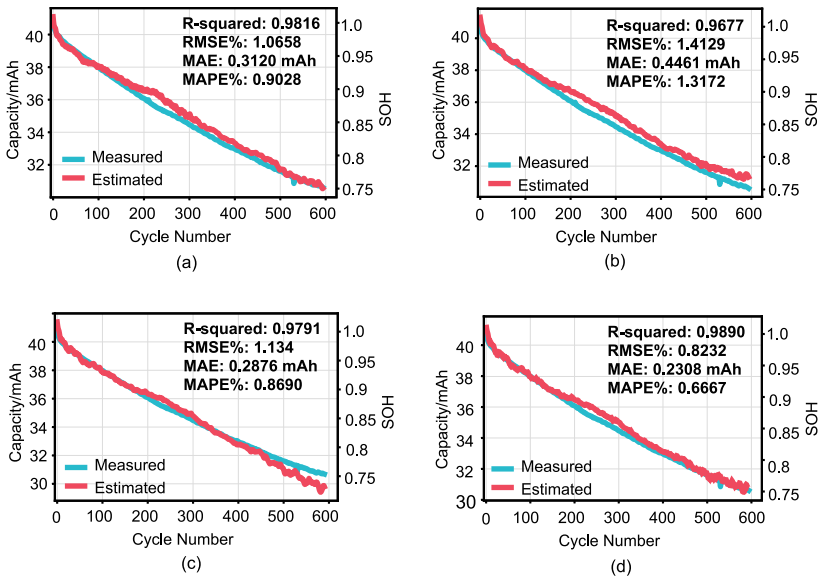

Fig. 8. Capacity estimation results for T452, (a) State 1, (b) State 2, (c) State 3, (d) State 4.

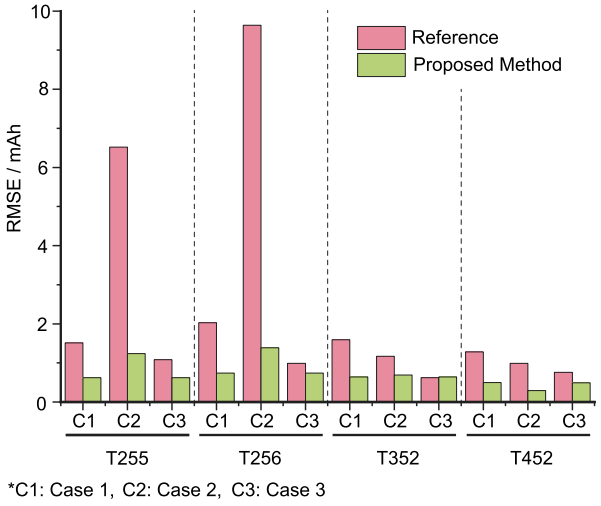

Fig. 9. Comparison of RMSE in three cases.

feature selection methods were more complex compared to the simpler and more efficient approach proposed in this study.

These comparative findings underscore that the combination of effective feature extraction, initial adjustment, and temperature feature fusion significantly enhances performance, showcasing the robustness of the proposed approach in achieving exceptional results.

4.2. Capacity estimation comparison cases

This subsection further validates the effectiveness and necessity of the proposed method by discussing four distinct cases. Each case demonstrates how the method addresses specific challenges and enhances performance in various contexts.

4.2.1. Verification of feature extraction - case 1

In Section 2, we utilized Spearman's correlation analysis to extract the imaginary impedance at 2.74 Hz as a feature. To validate its necessity, a comparative experiment involving all 120 features (both imaginary and real impedance) across 60 frequencies was conducted, with results presented in Fig. A.1 and Table A.1. Upon entering all EIS data into the model, the MAPE increased by an average relative percentage of approximately 153% (from a range of 1.3%–2.4% to 3.01%–7.39%), and the other three evaluation metrics also decreased to varying degrees. These results demonstrate that complex, high-dimensional EIS information can lead to information redundancy, preventing the model from directly learning knowledge related to battery aging and thus resulting in lower estimation accuracy.

Furthermore, we compared the time consumption during the model training process. Under the same hyper-parameters and using a Google Colab T4 GPU for three separate runs, the average training time with all EIS data was 74.2 s, while training with the proposed feature set reduced the average training time to 19.8 s, improving efficiency by over 73.30%. This demonstrates that utilizing a single frequency feature eliminates feature redundancy while preserving valid information, leading to optimal performance in both efficiency and accuracy. Additionally, the complexity of the data acquisition process is significantly reduced, enhancing the feasibility of the proposed method in practical applications.

4.2.2. Verification of initial adjustment - case 2

In Section 2.3, the analysis of the raw data revealed significant variability and a wide distribution. This observation led to the proposal of initial adjustment to enable the model to concentrate more on the battery aging process rather than the impacts of their initial values. Verification was conducted on the data both with and without initial adjustment, and the results are displayed in Figs. 9–11 and Table A.2. The data without initial adjustment produced very unsatisfactory estimation results. Specifically, the MAPE reached an error of 35.25% on battery T256, which is 30% higher than in the reference scenario. Furthermore, the average MAPE values for the estimation results of four batteries were calculated under both conditions. The average MAPE without the initial adjustment was 15.65%, whereas after applying the initial adjustment method, the average dropped to 2.87%. Therefore, it is concluded that the initial adjustment not only preserves the real correlation between the imaginary part of impedance and capacity but also effectively reduces the impact of differences among cells on capacity estimation, further improving its accuracy.

4.2.3. Verification of temperature feature fusion - case 3

In Section 3, a feature fusion unit was integrated between the encoder and decoder structures of the basic transformer model to include the temperature dimension. To assess the effectiveness of this addition,

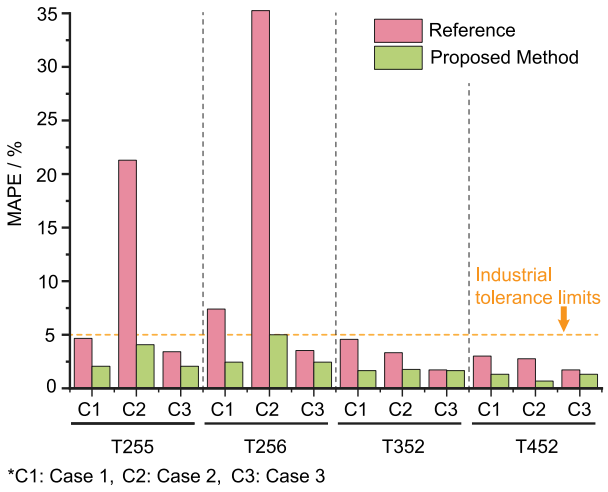

Fig. 10. Comparison of MAPE in three cases.

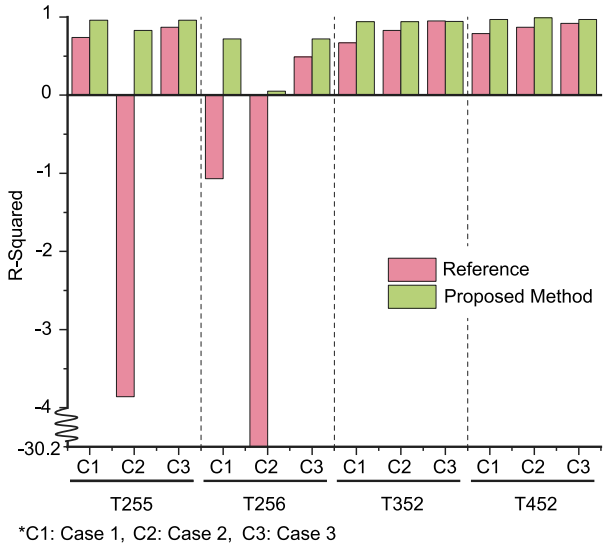

Fig. 11. Comparison of R^2 in three cases.

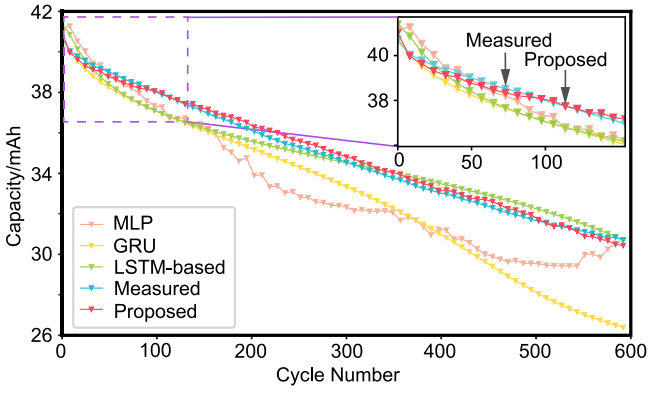

Fig. 12. Capacity estimation comparison across algorithms.

comparative estimations were performed, with results detailed in Figs. 9–11 and Table A.3. From which we can conclude that the inclusion of the temperature fusion unit markedly improved the accuracy of battery capacity estimation. With the decrease in MAPE from 1.73%–3.54% to 1.31%–2.45%, representing an average relative reduction of approximately 28%. Notably, for battery T352, the impact of the temperature fusion unit was less distinct. This can be attributed to the normalization of temperature scalars at 25, 35, and 45 degrees, where the normalized data for 35 degrees approached zero, thereby reducing the beneficial effects of the temperature fusion unit at this temperature. Nevertheless, as demonstrated in Figs. 9–11 and Table A.3, integrating the feature fusion unit enhanced battery capacity estimation. Additionally, should further data related to battery aging — such as DoD and C-rate — become available, it could be seamlessly integrated into the battery aging model via the feature fusion unit.

Table 4
Performance metrics comparison: Different algorithms.

Algorithms	RMSE (mAh)	MAE (mAh)	MAPE (%)	R^2
MLP	1.72	1.54	4.54	0.61
GRU	2.21	1.82	5.53	0.35
LSTM-based	0.54	0.47	1.33	0.96
Proposed	0.23	0.20	0.59	0.99

4.2.4. Comparison of benchmark algorithms

This section compares traditional deep learning algorithms and the proposed method under the condition of fully discharged T452 cells. Additionally, an LSTM-based algorithm incorporating temperature features was developed to compare the capacity estimation results. As illustrated in Fig. 12, the estimation results of different algorithms vary significantly. Among them, the Multi-Layer Perceptron (MLP) and Gated Recurrent Unit (GRU) algorithms demonstrate poor performance, providing accurate estimates only in the early stages of battery life. However, during the mid and late stages, their predictions deviate considerably from the measured values. Table 4 shows that the MAPE values for these two algorithms are around 5%. In contrast, both the LSTM-based and Transformer-based algorithms, which integrate temperature features, yield superior results. Fig. 12 demonstrates that these algorithms perform well across the entire battery lifespan. Moreover, as shown in Table 4, the R^2 values of the estimated battery degradation curves using these two methods exceed 96%, with the proposed method achieving an R^2 of 0.99 and a MAPE of only 0.59%. The comparative analysis of different algorithms further validates the superior performance in capacity estimation.

5. Conclusion

This paper introduces a feasible framework for estimating battery capacity, encompassing feature extraction, data processing, and an aging model applicable to batteries operating under various temperatures and working states. A temperature-enhanced model is established using features extracted through an EIS-Capacity correlation analysis method. An initial adjustment method is proposed to shield the model from dataset variability. The proposed method has been validated across three operating temperatures and six battery states covering the entire charge–discharge cycle. Compared to using broadband EIS as input, the extracted feature reduces the capacity estimation error by 5%. The results demonstrate that we can achieve more precise estimations by using 1/120th of the original data volume. The proposed initial adjustment method accurately captures the relative evolution trends of both features and capacity within datasets that exhibit significant variability and broad distributions. Compared to unprocessed data, this approach reduces the MAE by 8.3 mAh and the MAPE by 30.3%. A temperature-enhanced battery degradation model is introduced, integrating a temperature feature unit to improve estimation accuracy under varying temperature conditions. Compared to models without temperature fusion, the proposed approach achieves a 1.4% reduction in MAPE and a 0.4 mAh reduction in RMSE. With its low data requirements and robust features, this method is also well-suited for large-scale offline diagnostics, and holds promise for future online deployment in advanced battery management systems.

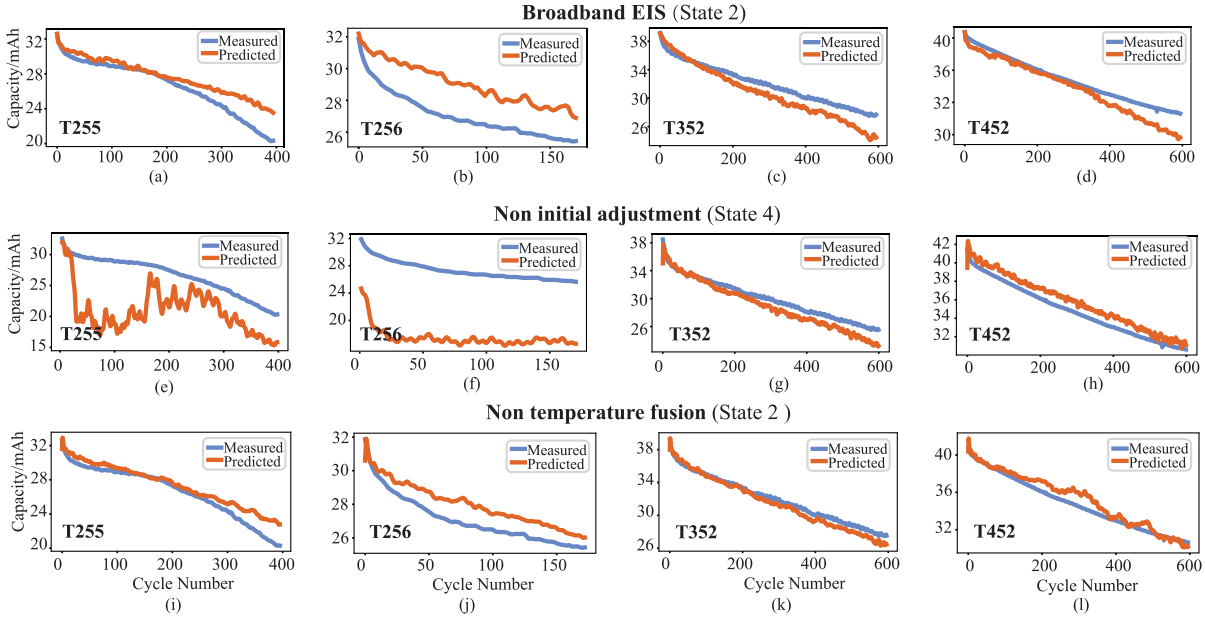

Fig. A.1. Capacity estimation comparison cases results. (a)–(d) show the estimation results for Case 1 using Broadband EIS as features; (e)–(h) present the estimation results for Case 2 without the initial adjustment method; (i)–(l) display the estimation results for Case 3 without the inclusion of the temperature fusion unit.

Table A.1
Performance metrics comparison: Case 1.

Case 1	Cell	RMSE (mAh)	MAE (mAh)	MAPE (%)	R^2
Broadband EIS	T255	1.51	1.10	4.66	0.74
	T256	2.03	1.99	7.39	−1.07
	T352	1.59	1.39	4.57	0.67
	T452	1.28	0.99	3.01	0.79
2.74 Hz (-Im[Z])	T255	0.62	0.53	2.05	0.96
	T256	0.74	0.66	2.44	0.72
	T352	0.64	0.49	1.65	0.94
	T452	0.49	0.44	1.32	0.97

Table A.2
Performance metrics comparison: Case 2.

Case 2	Cell	RMSE (mAh)	MAE (mAh)	MAPE (%)	R^2
Non initial adjustment	T255	6.52	5.72	21.29	−3.85
	T256	9.64	9.57	35.25	−30.20
	T352	1.17	1.01	3.31	0.83
	T452	0.99	0.96	2.75	0.87
Initial adjustment	T255	1.23	0.98	4.07	0.83
	T256	1.39	1.33	4.99	0.01
	T352	0.69	0.54	1.76	0.94
	T452	0.29	0.23	0.67	0.99

Table A.3
Performance metrics comparison: Case 3.

Case 3	Cell	RMSE (mAh)	MAE (mAh)	MAPE (%)	R^2
Non temperature fusion	T255	1.08	0.82	3.41	0.87
	T256	0.99	0.95	3.53	0.49
	T352	0.62	0.52	1.73	0.95
	T452	0.75	0.60	1.72	0.92
Temperature fusion	T255	0.62	0.53	2.05	0.96
	T256	0.74	0.66	2.44	0.72
	T352	0.64	0.49	1.65	0.94
	T452	0.49	0.44	1.32	0.97

Table A.4
The complete list of abbreviations.

Abbreviation	Description	Abbreviation	Description
SOH	State of Health	EIS	Electrochemical Impedance Spectroscopy
SOC	State of Charge	DC	Direct Current
ECM	Equivalent Circuit Model	SCC	Spearman's rank Correlation Coefficient
CNN	Convolutional Neural Networks	DoD	Depth of Discharge
RNN	Recurrent neural network	FNN	Forward Neural Network
LSTM	Long Short-Term Memory	MAE	Mean Absolute Error
GAN	Generative Adversarial Networks	RMSE	Root Mean Square Error
GPR	Gaussian Process Regression	MAPE	Mean Absolute Percentage Error
MLP	Multi-Layer Perceptron	GRU	Gated Recurrent Unit

CRediT authorship contribution statement

Ruijun Liu: Writing – original draft, Software, Methodology, Investigation, Formal analysis, Conceptualization. **Dayu Zhang:** Writing – review & editing, Validation, Methodology, Conceptualization. **Lu Wang:** Writing – review & editing, Visualization, Software, Formal analysis. **Chunting Chris Mi:** Writing – review & editing, Resources, Investigation. **Pavol Bauer:** Supervision, Funding acquisition, Conceptualization. **Zian Qin:** Writing – review & editing, Supervision, Methodology, Funding acquisition.

Declaration of competing interest

The authors declare that they have no known competing financial interests or personal relationships that could have appeared to influence the work reported in this paper.

Appendix. Supplementary information

See Fig. A.1 and Tables A.1–A.4.

Data availability

The authors do not have permission to share data.

References

[1] N. Collath, B. Tepe, S. Englberger, A. Jossen, H. Hesse, Aging aware operation of lithium-ion battery energy storage systems: A review, J. Energy Storage 55 (2022) 105634, http://dx.doi.org/10.1016/j.est.2022.105634.

[2] J. Zhu, W. Xu, M. Knapp, M.S.D. Darma, L. Mereacre, P. Su, W. Hua, X. Liu-Théato, H. Dai, X. Wei, et al., A method to prolong lithium-ion battery life during the full life cycle, Cell Rep. Phys. Sci. 4 (7) (2023) http://dx.doi.org/10.1016/j.xcrp.2023.101464.

[3] L. Ungurean, G. Cârstoiu, M.V. Micea, V. Groza, Battery state of health estimation: a structured review of models, methods and commercial devices, Int. J. Energy Res. 41 (2) (2017) 151–181, http://dx.doi.org/10.1002/er.3598.

[4] L. Yao, S. Xu, A. Tang, F. Zhou, J. Hou, Y. Xiao, Z. Fu, A review of lithium-ion battery state of health estimation and prediction methods, World Electr. Veh. J. 12 (3) (2021) 113, http://dx.doi.org/10.3390/wevj12030113.

[5] J.S. Edge, S. O'Kane, R. Prosser, N.D. Kirkaldy, A.N. Patel, A. Hales, A. Ghosh, W. Ai, J. Chen, J. Yang, S. Li, M.-C. Pang, L. Bravo Diaz, A. Tomaszewska, M.W. Marzook, K.N. Radhakrishnan, H. Wang, Y. Patel, B. Wu, G.J. Offer, Lithium ion battery degradation: what you need to know, Phys. Chem. Chem. Phys. 23 (14) (2021) 8200–8221, http://dx.doi.org/10.1039/D1CP00359C.

[6] X. Hu, L. Xu, X. Lin, M. Pecht, Battery lifetime prognostics, Joule 4 (2) (2020) 310–346, http://dx.doi.org/10.1016/j.joule.2019.11.018.

[7] R. Xiong, Y. Pan, W. Shen, H. Li, F. Sun, Lithium-ion battery aging mechanisms and diagnosis method for automotive applications: Recent advances and perspectives, Renew. Sustain. Energy Rev. 131 (2020) 110048, http://dx.doi.org/10.1016/j.rser.2020.110048.

[8] Y. Wang, J. Tian, Z. Sun, L. Wang, R. Xu, M. Li, Z. Chen, A comprehensive review of battery modeling and state estimation approaches for advanced battery management systems, Renew. Sustain. Energy Rev. 131 (2020) 110015, http://dx.doi.org/10.1016/j.rser.2020.110015.

[9] F. Wang, Z. Zhai, Z. Zhao, Y. Di, X. Chen, Physics-informed neural network for lithium-ion battery degradation stable modeling and prognosis, Nat. Commun. 15 (1) (2024) 4332, http://dx.doi.org/10.1038/s41467-024-48779-z.

[10] J. de Hoog, J.-M. Timmermans, D. Ioan-Stroe, M. Swierczynski, J. Jaguemont, S. Goutam, N. Omar, J. Van Mierlo, P. Van Den Bossche, Combined cycling and calendar capacity fade modeling of a Nickel–Manganese–Cobalt oxide cell with real-life profile validation, Appl. Energy 200 (2017) 47–61, http://dx.doi.org/10.1016/j.apenergy.2017.05.018.

[11] W. Vermeer, G.R.C. Mouli, P. Bauer, A comprehensive review on the characteristics and modeling of lithium-ion battery aging, IEEE Trans. Transp. Electrif. 8 (2) (2021) 2205–2232, http://dx.doi.org/10.1109/TTE.2021.3138357.

[12] S. Wang, S. Zhang, S. Wen, C. Fernandez, An accurate state-of-charge estimation of lithium-ion batteries based on improved particle swarm optimization-adaptive square root cubature kalman filter, J. Power Sources 624 (2024) 235594, http://dx.doi.org/10.1016/j.jpowsour.2024.235594.

[13] R. Xiong, L. Li, Z. Li, Q. Yu, H. Mu, An electrochemical model based degradation state identification method of lithium-ion battery for all-climate electric vehicles application, Appl. Energy 219 (2018) 264–275, http://dx.doi.org/10.1016/j.apenergy.2018.03.053.

[14] M.A. Rahman, S. Anwar, A. Izadian, Electrochemical model parameter identification of a lithium-ion battery using particle swarm optimization method, J. Power Sources 307 (2016) 86–97, http://dx.doi.org/10.1016/j.jpowsour.2015.12.083.

[15] S. Wang, Q. Dang, Z. Gao, B. Li, C. Fernandez, F. Blaabjerg, An innovative square root - untraced Kalman filtering strategy with full-parameter online identification for state of power evaluation of lithium-ion batteries, J. Energy Storage 104 (2024) 114555, http://dx.doi.org/10.1016/j.est.2024.114555.

[16] S. Wang, C. Wang, P. Takyi-Aninakwa, S. Jin, C. Fernandez, Q. Huang, An improved parameter identification and radial basis correction-differential support vector machine strategies for state-of-charge estimation of urban-transportation-electric-vehicle lithium-ion batteries, J. Energy Storage 80 (2024) 110222, http://dx.doi.org/10.1016/j.est.2023.110222.

[17] J. Zhao, X. Han, M. Ouyang, A.F. Burke, Specialized deep neural networks for battery health prognostics: Opportunities and challenges, J. Energy Chem. 87 (2023) 416–438, http://dx.doi.org/10.1016/j.jechem.2023.08.047.

[18] L. Zhang, H. Peng, Z. Ning, Z. Mu, C. Sun, Comparative research on RC equivalent circuit models for lithium-ion batteries of electric vehicles, Appl. Sci. 7 (10) (2017) 1002, http://dx.doi.org/10.3390/app7101002.

[19] Y. Zhang, Q. Tang, Y. Zhang, J. Wang, U. Stimming, A.A. Lee, Identifying degradation patterns of lithium ion batteries from impedance spectroscopy using machine learning, Nat. Commun. 11 (1) (2020) 1706, http://dx.doi.org/10.1038/s41467-020-15235-7.

[20] Q. Wang, M. Ye, X. Cai, D.U. Sauer, W. Li, Transferable data-driven capacity estimation for lithium-ion batteries with deep learning: A case study from laboratory to field applications, Appl. Energy 350 (2023) 121747, http://dx.doi.org/10.1016/j.apenergy.2023.121747.

[21] W. Li, N. Sengupta, P. Dechent, D. Howey, A. Annaswamy, D.U. Sauer, Online capacity estimation of lithium-ion batteries with deep long short-term memory networks, J. Power Sources 482 (2021) 228863, http://dx.doi.org/10.1016/j.jpowsour.2020.228863.

[22] Y. Che, D.-I. Stroe, X. Hu, R. Teodorescu, Semi-supervised self-learning-based lifetime prediction for batteries, IEEE Trans. Ind. Inform. 19 (5) (2023) 6471–6481, http://dx.doi.org/10.1109/TII.2022.3206776.

[23] K. Liu, Z. Wei, C. Zhang, Y. Shang, R. Teodorescu, Q.-L. Han, Towards long lifetime battery: AI-based manufacturing and management, IEEE/CAA J. Autom. Sin. 9 (7) (2022) 1139–1165, http://dx.doi.org/10.1109/JAS.2022.105599.

[24] N. Yang, Z. Song, H. Hofmann, J. Sun, Robust state of health estimation of lithium-ion batteries using convolutional neural network and random forest, J. Energy Storage 48 (2022) 103857, http://dx.doi.org/10.1016/j.est.2021.103857.

[25] A. Vaswani, N. Shazeer, N. Parmar, J. Uszkoreit, L. Jones, A.N. Gomez, Ł. Kaiser, I. Polosukhin, Attention is all you need, Adv. Neural Inf. Process. Syst. 30 (2017) https://proceedings.neurips.cc/paper_files/paper/2017/file/3f5ee243547dee91fbd053c1c4a845aa-Paper.pdf.

[26] K. Luo, H. Zheng, Z. Shi, A simple feature extraction method for estimating the whole life cycle state of health of lithium-ion batteries using transformer-based neural network, J. Power Sources 576 (2023) 233139, http://dx.doi.org/10.1016/j.jpowsour.2023.233139.

[27] T. Bai, H. Wang, Convolutional transformer-based multiview information perception framework for lithium-ion battery state-of-health estimation, IEEE Trans. Instrum. Meas. 72 (2023) 1–12, http://dx.doi.org/10.1109/TIM.2023.3300451.

[28] S. Kim, Y.Y. Choi, J.-I. Choi, Impedance-based capacity estimation for lithium-ion batteries using generative adversarial network, Appl. Energy 308 (2022) 118317, http://dx.doi.org/10.1016/j.apenergy.2021.118317.
[29] R. Xiong, L. Li, J. Tian, Towards a smarter battery management system: A critical review on battery state of health monitoring methods, J. Power Sources 405 (2018) 18–29, http://dx.doi.org/10.1016/j.jpowsour.2018.10.019.
[30] A. Eddahech, O. Briat, J.-M. Vinassa, Determination of lithium-ion battery state-of-health based on constant-voltage charge phase, J. Power Sources 258 (2014) 218–227, http://dx.doi.org/10.1016/j.jpowsour.2014.02.020.
[31] D. Zhang, Z. Wang, L. Peng, Z. Qin, Q. Wang, C. She, P. Bauer, Multi-step fast charging based state of health estimation of lithium-ion batteries, IEEE Trans. Transp. Electrif. 10 (3) (2024) 4640–4652, http://dx.doi.org/10.1109/TTE.2023.3322582.
[32] X. Bian, Z. Wei, W. Li, J. Pou, D.U. Sauer, L. Liu, State-of-health estimation of lithium-ion batteries by fusing an open circuit voltage model and incremental capacity analysis, IEEE Trans. Power Electron. 37 (2) (2022) 2226–2236, http://dx.doi.org/10.1109/TPEL.2021.3104723.
[33] S. Fu, S. Tao, H. Fan, K. He, X. Liu, Y. Tao, J. Zuo, X. Zhang, Y. Wang, Y. Sun, Data-driven capacity estimation for lithium-ion batteries with feature matching based transfer learning method, Appl. Energy 353 (2024) 121991, http://dx.doi.org/10.1016/j.apenergy.2023.121991.
[34] P. Mohtat, S. Lee, J.B. Siegel, A.G. Stefanopoulou, Comparison of expansion and voltage differential indicators for battery capacity fade, J. Power Sources 518 (2022) 230714, http://dx.doi.org/10.1016/j.jpowsour.2021.230714.
[35] W. Hu, Y. Peng, Y. Wei, Y. Yang, Application of electrochemical impedance spectroscopy to degradation and aging research of lithium-ion batteries, J. Phys. Chem. C 127 (9) (2023) 4465–4495, http://dx.doi.org/10.1021/acs.jpcc.3c00033.
[36] P.K. Jones, U. Stimming, A.A. Lee, Impedance-based forecasting of lithium-ion battery performance amid uneven usage, Nat. Commun. 13 (1) (2022) 4806, http://dx.doi.org/10.1038/s41467-022-32422-w.
[37] B. Jiang, J. Zhu, X. Wang, X. Wei, W. Shang, H. Dai, A comparative study of different features extracted from electrochemical impedance spectroscopy in state of health estimation for lithium-ion batteries, Appl. Energy 322 (2022) 119502, http://dx.doi.org/10.1016/j.apenergy.2022.119502.
[38] M. Faraji-Niri, M. Rashid, J. Sansom, M. Sheikh, D. Widanage, J. Marco, Accelerated state of health estimation of second life lithium-ion batteries via electrochemical impedance spectroscopy tests and machine learning techniques, J. Energy Storage 58 (2023) 106295, http://dx.doi.org/10.1016/j.est.2022.106295.
[39] R. He, Y. He, W. Xie, B. Guo, S. Yang, Comparative analysis for commercial li-ion batteries degradation using the distribution of relaxation time method based on electrochemical impedance spectroscopy, Energy 263 (2023) 125972, http://dx.doi.org/10.1016/j.energy.2022.125972.
[40] X. Bian, L. Liu, J. Yan, Z. Zou, R. Zhao, An open circuit voltage-based model for state-of-health estimation of lithium-ion batteries: Model development and validation, J. Power Sources 448 (2020) 227401, http://dx.doi.org/10.1016/j.jpowsour.2019.227401.
[41] D. Cui, Z. Wang, P. Liu, S. Wang, Z. Zhang, D.G. Dorrell, X. Li, Battery electric vehicle usage pattern analysis driven by massive real-world data, Energy 250 (2022) 123837, http://dx.doi.org/10.1016/j.energy.2022.123837.
[42] J. Zhu, Y. Wang, Y. Huang, R. Bhushan Gopaluni, Y. Cao, M. Heere, M.J. Mühlbauer, L. Mereacre, H. Dai, X. Liu, et al., Data-driven capacity estimation of commercial lithium-ion batteries from voltage relaxation, Nat. Commun. 13 (1) (2022) 2261, http://dx.doi.org/10.1038/s41467-022-29837-w.
[43] S.S. Shapiro, M.B. Wilk, An analysis of variance test for normality (complete samples), Biometrika 52 (3–4) (1965) 591–611, http://dx.doi.org/10.2307/2333709.
[44] J.H. Zar, Spearman rank correlation, Encycl. Biostat. 7 (2005) http://dx.doi.org/10.1002/0470011815.b2a15150.
[45] Y. Liu, Q. Li, K. Wang, Revealing the degradation patterns of lithium-ion batteries from impedance spectroscopy using variational auto-encoders, Energy Storage Mater. 69 (103394) (2024) http://dx.doi.org/10.1016/j.ensm.2024.103394.
[46] X. Du, J. Meng, Y. Amirat, F. Gao, M. Benbouzid, Feature selection strategy optimization for lithium-ion battery state of health estimation under impedance uncertainties, J. Energy Chem. 101 (2025) 87–98, http://dx.doi.org/10.1016/j.jechem.2024.09.032.
[47] Z. Liu, Y. Sun, Y. Li, Y. Liu, Y. Chen, Y. Zhang, Lithium-ion battery health prognosis via electrochemical impedance spectroscopy using CNN-BiLSTM model, J. Mater. Inform. 4 (2) (2024) http://dx.doi.org/10.20517/jmi.2024.09.
[48] Z. Song, N. Yang, X. Lin, F. Pinto Delgado, H. Hofmann, J. Sun, Progression of cell-to-cell variation within battery modules under different cooling structures, Appl. Energy 312 (2022) 118836, http://dx.doi.org/10.1016/j.apenergy.2022.118836.
[49] I. Zilberman, S. Ludwig, A. Jossen, Cell-to-cell variation of calendar aging and reversible self-discharge in 18650 nickel-rich, silicon–graphite lithium-ion cells, J. Energy Storage 26 (2019) 100900, http://dx.doi.org/10.1016/j.est.2019.100900.
[50] R. Liu, D. Zhang, Z. Li, P. Bauer, Z. Qin, Feature extraction from electrochemical impedance spectroscopy for state of health estimation of lithium-ion batteries under different temperatures, in: 2024 IEEE 10th International Power Electronics and Motion Control Conference, IPEMC2024-ECCE Asia, 2024, pp. 3374–3378, http://dx.doi.org/10.1109/IPEMC-ECCEAsia60879.2024.10567365.
[51] Y. Zhang, Y.-F. Li, Prognostics and health management of lithium-ion battery using deep learning methods: A review, Renew. Sustain. Energy Rev. 161 (2022) 112282, http://dx.doi.org/10.1016/j.rser.2022.112282.